Computer Methods and Programs in Biomedicine 280 (2026) 109309

Contents lists available at ScienceDirect

Computer Methods and Programs in Biomedicine

journal homepage: https://www.sciencedirect.com/journal/computer-methods-and-programs-in-biomedicine

A robust topology optimization based biomechanical computational framework for patient-specific trabecular bone microstructure reconstruction

Zeyang Li [a,1], Xuanxuan Huang [a,1], Ziyun Ding [b], Carol Featherston [a], Sam L. Evans [a], Peter Zioupos [c], Zhangming Wu [a,*]

[a] School of Engineering, Cardiff University, Cardiff, CF24 3AA, Wales, UK
[b] School of Engineering, University of Birmingham, Birmingham, B15 2TT, UK
[c] School of Engineering, University of Hull, Hull, HU6 7RX, UK

ARTICLE INFO

Keywords:
Trabecular bone reconstruction
Robust topology optimization
Biomechanics-driven image processing
Gait load uncertainty

ABSTRACT

Background and Objective: Accurate reconstruction of trabecular bone microstructure is essential for understanding bone health and mechanical competence. Low-resolution computed tomography images, however, lack the detailed information that is needed to depict fine trabecular architecture. This study aims to develop a computational framework that reconstructs subject-specific trabecular microstructure with improved accuracy and stability by incorporating mechanical and biological variability inherent in bone adaptation.

Methods: A robust topology optimization framework was developed to predict trabecular morphology from low-resolution images. The method incorporates uncertainty in loading and biological response during bone remodeling. To reduce sensitivity to variations in boundary forces, a superposition strategy was used to estimate local mechanical stimuli within each volume of interest. The predicted microstructure was compared against high-resolution images of rabbit bone for validation, and subsequently applied to human lower-limb bone images. Quantitative assessments included geometric similarity and evaluation of mechanical anisotropy.

Results: The reconstructed trabecular regions showed close agreement with high-resolution microstructural images in the animal validation study, capturing fine branching and connectivity patterns. In human bone, the predicted morphology was consistent with expected statistical distributions of trabecular thickness, spacing, and orientation. The framework demonstrated high computational precision and stability, producing anisotropic mechanical properties aligned with physiological loading patterns.

Conclusions: This computational approach enables patient-specific reconstruction of trabecular microstructure from low-resolution imaging with improved robustness and reduced computational cost. The framework shows potential for supporting clinical assessment and for advancing multi-scale investigations of bone mechanics.

1. Introduction

The study of trabecular bone microstructure is one of the focuses of orthopedic mechanics research. The determination of trabecular bone microstructure in addition to its mineral density via Computed Tomography (CT) or other high-resolution imaging techniques plays an increasingly important role in the clinical diagnosis of bone-related diseases, e.g., osteoporosis, hyperostosis, and osteoarthritis. Previous studies have shown that the density of cancellous bone material, named bone mineral density (BMD) only determines 60% ∼ 80% of bone strength [1], whereas more than 90% of the mechanical response of bone tissue and its anisotropy property depends on the trabecular microstructure [2]. In light of this, the trabecular bone microstructure has garnered extensive attention in clinical diagnosis, artificial implant design, and multi-level bone mechanics research. A deep understanding of local variations in trabecular bone microstructure is essential for evaluating patterns of bone loss associated with aging and skeletal disorders, offering valuable insights into osteoporosis and fracture risk prediction [3].

Current methods for bone assessment primarily rely on medical imaging techniques. Dual-energy X-ray absorptiometry (DXA), the clinical standard for diagnosing osteoporosis, offers limited imaging information for bone strength assessment, as it measures only the average

* Corresponding author.
E-mail address: wuz12@cardiff.ac.uk (Z. Wu).
[1] These two authors contributed equally to this work.

https://doi.org/10.1016/j.cmpb.2026.109309
Received 3 December 2025; Received in revised form 25 February 2026; Accepted 6 March 2026
Available online 12 March 2026

bone mineral density (BMD) within each volume of interest [4]. Computed tomography (CT) is extensively used for its ability to produce detailed 3D bone information and effectively visualize central skeletal regions, such as the proximal femur and lumbar spine, making it a valuable tool for bone health diagnosis [5]. However, clinical CT scans typically operate at relatively low resolution (300 μm ∼ 600 μm) to minimize radiation exposure, making it challenging to capture the fine structures of trabecular branches, which typically range from 100 μm ∼ 200 μm in thickness. This resolution limitation significantly hampers the accurate diagnosis of osteoporosis, hyperplasia, and other bone-related conditions.

High-resolution imaging modalities, such as high-resolution peripheral quantitative computed tomography (HR-pQCT), micro-computed tomography (micro-CT), and magnetic resonance imaging (MRI), have advanced the assessment of bone microstructure by providing detailed information into geometry, trabecular connectivity, structural indices, and anisotropy [6,7]. HR-pQCT provides detailed imaging but is limited to peripheral skeletal regions, such as the wrist and ankle, while MRI can image central sites like the proximal femur, albeit with lower spatial resolution [6]. Micro-computed tomography (micro-CT) offers even higher resolution but involves significant radiation exposure, limiting its clinical applicability. Recent advancements in imaging have improved MRI's capability to evaluate bone strength and osteoporosis, particularly at critical sites like the proximal femur [7]. However, limitations such as lower spatial resolution, extended acquisition times, high costs, and, in some cases, excessive radiation exposure continue to hinder the widespread clinical adoptions of these HR imaging techniques [7,8].

Early approaches to enhancing low-resolution CT (LR-CT) images primarily used standard image sharpening techniques [9,10]. However, these methods offered limited accuracy and adaptability, as they often lacked patient-specific information essential for accurate bone health assessment [11]. In recent years, the advancements in computer science, particularly in artificial intelligence and deep learning, have also significantly improved the processing and analysis of medical images. With this, researchers have successfully generated super-resolution (SR) images with remarkable details (10 μm ∼ 50 μm) for biomedical tissues [12,13]. These deep learning-based approaches have demonstrated the ability to reconstruct trabecular bone microstructure from low-resolution (LR) CT images, offering clearer visualization and improved diagnostic potential. Despite these advancements, significant challenges remain. Deep learning methods often require extensive training datasets and depend on high initial CT resolution (approximately 100 μm) to achieve accurate results. Additionally, the computational costs and hardware demands are considerable, which hinders their integration into routine clinical workflows. To address these limitations, there remains ongoing demands to develop efficient, lightweight, and cost-effective image refinement techniques that can deliver high-quality results while meeting practical requirements for clinical applications.

Inspired by the biomechanical principles and self-optimization characteristics of bone tissues, researchers have explored structural topology optimization (TO) methods for providing a new paradigm to reconstruct trabecular bone microstructure in clinical practice [4,7,14]. According to Wolff's law, trabecular bone dynamically adjust its architecture to better affording external loads through bone remodeling processes [15–17]. This adaptability closely resembles the optimal compliance solutions provided by a topology optimization process [4]. Jang's early work [5] demonstrated the potential of 2D topology optimization for reconstructing trabecular bone in the proximal femur, producing numerical results that closely aligned with the natural trabecular orientation and anisotropic properties. Afterwards, Kim et al. [4,14] advanced TO methods to improve the representation of local trabecular branches while achieving high spatial accuracy and structural fidelity. Compared to neural network-based image processing, TO-based methods are computationally efficient, do not require extensive training datasets, and are more suitable for patient-specific bone configurations in routine clinical applications. These advantages position the TO-based method as a promising technique for precise and practical trabecular bone assessment in clinical applications.

Despite its potential, the use of TO-based methods for trabecular bone microstructure reconstruction remains in its early stages. For instance, the current TO-based methods do not adequately account for physiological stochasticity and other sources of uncertainty, e.g., gait force error, patient-disease error. While the analogy between bone remodeling and structural topology optimization is well-established [18], the bone remodeling process is also regulated by diverse cellular activities influenced by mechanical and biological uncertainties [19,20]. Reconstructing trabecular bone simply as a stiffness-optimized structure using deterministic single-objective TO, as demonstrated in previous studies [4,7,14], may fail to fully align with Wolff's law, omitting critical patient-specific features. Incorporating the stochastic nature of biological activities into TO algorithms could yield more physiologically realistic trabecular structures [21].

According to Wolff's law, bone remodels itself to adapt to external loads. Bone adaptation to applied load conditions [19,22] underscores the significance of boundary forces in influencing the quality and accuracy of reconstructed trabecular microstructure. Previous studies typically extracted 2 ∼ 3 representative loads from gait cycles based on biomechanical experience, using weighted arithmetic means to approximate boundary forces [23–25]. While this approach reduces computational demands, it lacks the precision required to capture detailed trabecular refinement. Moreover, gait abnormalities in orthopedic patients often deviate significantly from normal patterns, introducing large errors into such weighted averages. This highlights the pressing need for more robust methods to define dynamic bone boundary loads. From this perspective, bone reconstruction that accounts for ‘‘uncertain factors'' may achieve greater physiological authenticity compared to traditional ‘‘maximum stiffness" topology optimization-based methods.

In this work, we introduce a biomechanical computational framework based on robust topology optimization (RTO) to reconstruct trabecular bone microstructures from low-resolution CT images. Unlike traditional reconstruction techniques that rely on image-based bone data processing, this RTO-based approach directly optimizes structural performance under uncertainty by minimizing both the expected value and variance of the performance. Integrating RTO into bone reconstruction enables the systematic consideration of patient-specific uncertainties, such as variations in gait force statistics and disease-induced defects. As a result, the reconstructed bone structures not only achieve accurate overall stiffness and morphology but also demonstrate enhanced stability under varying loading conditions. This feature aligns with the natural adaptability of biological tissues to complex mechanical environments, making the model closer to the geometric characteristics of real bones. This efficient RTO-based computational framework demonstrates strong potential for integration into clinical practice as a lightweight plugin for personalized diagnosis and treatment. Furthermore, its stochastic foundation provides a scalable computational framework for incorporating a broader range of mechanical and biological uncertainties, supporting the development of more reliable and adaptable bone reconstruction models in future studies.

2. Methods

Based on robust topology optimization (RTO) methods [26–29], the proposed computational method extends its capability beyond the existing typical TO-based bone reconstruction from low-resolution CT images [14]. It further incorporates a range of biomechanical conditions and uncertainties, particularly those arising from the stochastic nature of bone remodeling and variations in gait loading patterns. Through accounting for these uncertain factors, the framework provides a more accurate and reliable approach to trabecular microstructure reconstruction. The detailed workflow for this computational framework is outlined in three key steps, as illustrated in Fig. 1.

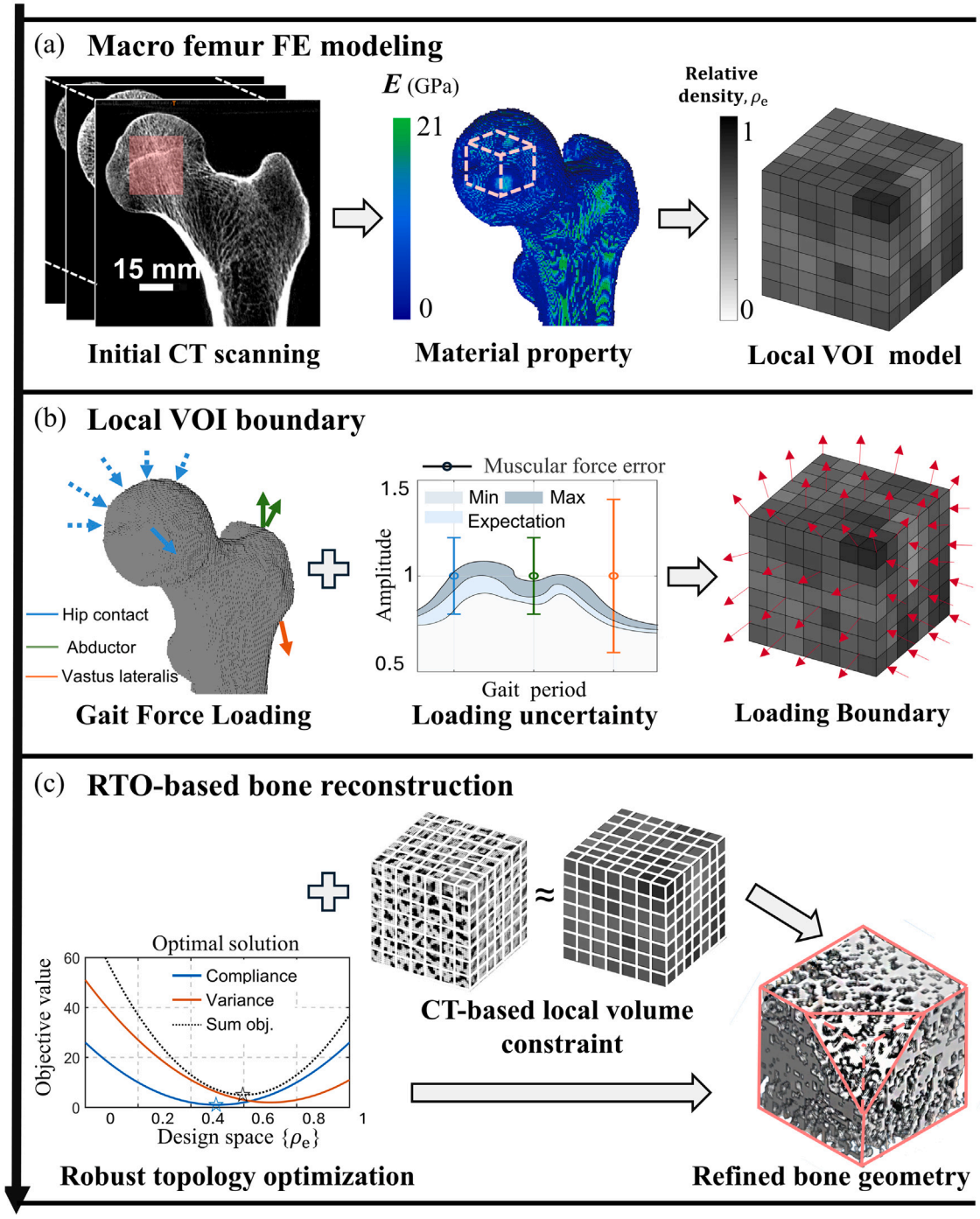

Fig. 1. Bone reconstruction workflow: The topological units are selected and developed based on the macro FE model constructed from the low resolution CT scan as step (a). Then, the corresponding loading conditions and uncertainty for the VOI are evaluated as step (b). Step (c) proposes the reconstruction process of high resolution bone geometry by the robust topology optimization, coupled with multiple local volume constraints referring to the original CT images. The final refined bone geometry is demonstrated with a sectional view at its corner.

- STEP 1: Construction of Macroscale Femoral Mesh. Firstly, a macroscale femoral mesh model is developed from the proximal segment of low resolution computerized tomography (LR CT) images of a clinical bone sample (as shown in Appendix A). The mesh size and multi-resolution bone mineral density (BMD) are determined using patient-specific factors, including age, gender, health status, and CT scanning parameters such as pixel values and Hounsfield units. Based on this data, elemental material properties are calculated and assigned to each element in the mesh. To simulate the physiological loading conditions in the finite element (FE) model, gait patterns are analyzed to estimate the forces acting on the femur. A finite element (FE) analysis is then performed to compute the resulting displacement and stress fields. To reduce computational cost, volumes of interest (VOIs) – where are clinically concerned regions such as the femoral head – are selected instead of modeling the entire femur. The displacement field within each VOI is extracted for use in the subsequent steps of the modeling and analysis.
- STEP 2: VOI Refinement and Boundary Force Estimation. Each VOI is further refined and re-meshed into smaller topological

elements for the purpose of detailed bone reconstruction. The effective boundary forces acting on the outer surface of the refined VOI are re-computed and updated based on the results from the original FEM model. The updated forces are then applied in the subsequent topology optimization process. Additionally, potential errors arising from uncertainties in gait-induced loading are accounted for during this step to enhance the robustness of the optimization.

- STEP 3: Bone Microstructure Reconstruction via Robust Topology Optimization (RTO). A robust topology optimization (RTO) procedure, which incorporates local volume constraints and accounts for uncertainties in gait-induced loading, is applied to reconstruct the trabecular bone microstructure within each refined VOI. This multi-objective RTO process minimizes a weighted sum of compliance and its variation to simulate the natural self-adaptive behavior of bone in maintaining mechanical stability under varying loads. Through an iterative process, the RTO-based biomechanical model generates a microstructural morphology that closely matches the original CT-derived structure, ensuring both mechanical efficiency and biomechanical reliability.

2.1. Construction of local VOI FE models

Following a series of pre-processing operations, CT images of a bone structure are transformed into a 3D FE model consisting of a large number of topological units. Each unit represents the relative density ρ within a localized finite volume. In this study, a volume of interest from the femoral head (FH), a region of high diagnostic significance, was selected to analyze the detailed bone trabecular microstructure. As illustrated in Fig. 1, a cubic model was extracted from each VOI, with voxel dimensions matching the CT image resolution (0.6 mm × 0.6 mm × 0.6 mm). The bone mineral density (BMD) map of each VOI was calibrated using a reference bar and then converted into a relative density map through linear scaling between the minimum and maximum values. For each voxel, its grayscale intensity is correlated with the corresponding Hounsfield unit of the CT image. To capture the detailed trabecular branches and plate structures, the original VOI model was further refined by subdividing each voxel into smaller child voxels. These child voxels directly inherited the relative density of their parent and were subsequently optimized to reproduce the intricate features of the trabecular microstructure. This refinement process enabled the reconstruction of a higher-resolution VOI model, while preserving the morphological details of the original trabecular bone structure.

For consistency, the FE model employs a type of structural Hexahedron elements to compute mechanical objectives in the later stages of the analysis. Each element is assigned a homogeneous material property, with the Young's modulus calculated based on its bone mineral density, following the empirical relationships established by Verhulp et al. [30], as follows:

$$\begin{aligned} E_i &= 6850\rho_i^{1.49}, \text{when } \rho_i < 1.64 \text{ g cm}^{-3} \\ E_i &= 4293\rho_i^{2.39}, \text{when } \rho_i \geq 1.64 \text{ g cm}^{-3} \end{aligned} \tag{1}$$

where E_i, ρ_i represent effective Young's modulus and the BMD of element i, respectively. Based on this formulation, a cubic VOI-FEM model is established from the femoral head region of the macroscale FE model for subsequent microstructural reconstruction, as illustrated in Fig. 1(a).

2.2. The boundary conditions for local VOI FE model

The boundary loads applied to the VOI model play a critical role in determining the resulting trabecular architecture during the topology optimization process. To simulate physiologically realistic loading conditions, we derive a modified boundary load vector $\mathbf{F}$ for the local VOI model from the macro-scale femur FE model subjected to daily gait loading vector $\mathbf{F}^m$. This computation of boundary loads follows the general framework proposed by Kim et al. [31], under the assumption that the displacement field along the VOI surface in the local model closely approximates that of the corresponding region in the macro-scale femur model. The overall boundary processing workflow is illustrated in Fig. 1(b). Specifically, the applied loads are reconstructed from three principal musculoskeletal force groups acting on the proximal femur model during gait, as described by Heller et al. [32]: the hip contact force ($\mathbf{F}^{m,1}$), the abductor force ($\mathbf{F}^{m,2}$), and the vastus lateralis force ($\mathbf{F}^{m,3}$).

Regarding the macro femur model, the mechanical response of bone structure is governed by the following equilibrium equation as:

$$\mathbf{K}^m\mathbf{U}^m = \mathbf{F}^m \quad \Leftrightarrow \quad \begin{bmatrix} \mathbf{K}^m_{ss} & \mathbf{K}^m_{sl} & \mathbf{K}^m_{sg} \\ \mathbf{K}^m_{ls} & \mathbf{K}^m_{ll} & \mathbf{K}^m_{lg} \\ \mathbf{K}^m_{gs} & \mathbf{K}^m_{gl} & \mathbf{K}^m_{gg} \end{bmatrix} \begin{bmatrix} \mathbf{U}^m_s \\ \mathbf{U}^m_l \\ \mathbf{U}^m_g \end{bmatrix} = \begin{bmatrix} \mathbf{F}^m_s \\ \mathbf{F}^m_l \\ \mathbf{F}^m_g \end{bmatrix} \tag{2}$$

where $\mathbf{K}^m$ and $\mathbf{U}^m$ represent the global stiffness matrix and the nodal displacement vector of the macro-scale femur model, respectively. To facilitate the information extraction of the local VOI model, the global system is partitioned based on nodal location into three categories: (1) nodes on the outer surface surrounding the VOI (denoted by subscript s), (2) internal nodes within the VOI (subscript l), and (3) all other nodes in the femur model (subscript g). This block-wise decomposition of the stiffness matrix and corresponding vectors facilitates the effective extraction of the mechanical state at the VOI interface.

For each local VOI model, which is independently constructed for topology-based bone reconstruction, the mechanical behavior is described by:

$$\mathbf{U} = \mathbf{K}^{-1}\mathbf{F} \quad \Leftrightarrow \quad \begin{bmatrix} \mathbf{U}_s \\ \mathbf{U}_l \end{bmatrix} = \begin{bmatrix} \mathbf{K}_{ss} & \mathbf{K}_{sl} \\ \mathbf{K}_{ls} & \mathbf{K}_{ll} \end{bmatrix}^{-1} \begin{bmatrix} \mathbf{F}_s \\ \mathbf{F}_l \end{bmatrix} \tag{3}$$

where $\mathbf{K}$, $\mathbf{U}$, and $\mathbf{F}$ represent the local stiffness matrix, nodal displacement vector, and applied load vector of the VOI model, respectively. To ensure consistency with the macro-scale response, we assume that the displacement field on the VOI surface approximates that of the macro model [31], as such:

$$\mathbf{U}_s \approx \mathbf{U}^m_s = \mathbf{R}_s\mathbf{U}^m \tag{4}$$

where $\mathbf{R}_s$ is a Boolean selection matrix that extracts the degrees of freedom corresponding to VOI surface nodes from the global displacement vector. Moreover, no external loads are applied to the internal nodes of the VOI model, so the work imposes: $\mathbf{F}_l = \mathbf{0}$ in Eq. (3). In this way, the equivalent desired loading boundary $\mathbf{F}_s$ acting on the VOI surface is derived from Eqs. (3) and (4), as follows:

$$\begin{aligned} \mathbf{F}_s &= \mathbf{K}_{ss}\mathbf{U}_s + \mathbf{K}_{sl}\mathbf{U}_l \\ &\approx \mathbf{K}_{ss}\mathbf{U}_s - \mathbf{K}_{sl}\mathbf{K}_{ll}^{-1}\mathbf{K}_{ls}\mathbf{U}_s \end{aligned} \tag{5}$$

However, the displacement field $\mathbf{U}_s$ inherited from the macro-scale model includes rigid-body motion components that are not compatible with standalone VOI simulations. In the global femur model, such motions are constrained by surrounding anatomical structures and tissues. In contrast, the independent VOI model must explicitly constrain at least six degrees of freedom to eliminate rigid-body motion and maintain numerical stability during optimization. Applying the boundary force vector $\mathbf{F}_s$ directly, without adjustment, may result in artificial drift, unbalanced reaction forces, and inaccurate internal stress resultants.

To resolve this inconsistency, the rigid-body components are removed from the surface displacement field. A reference corner node on the VOI boundary is selected, and all its translational degrees of freedom are fixed to eliminate rigid-body translation. The corresponding rigid translation vector, denoted by $\mathbf{U}_{\text{fix}}$, is used to compute the corrected displacement and force boundary conditions as follows:

$$\begin{aligned} &\mathbf{U}_s = \mathbf{U}^m_s - \mathbf{U}_{\text{fix}} = (\mathbf{I} - \mathbf{R}_f)\mathbf{U}^m_s, \\ &\mathbf{F}_s \approx (\mathbf{K}_{ss} - \mathbf{K}_{sl}\mathbf{K}_{ll}^{-1}\mathbf{K}_{ls})(\mathbf{I} - \mathbf{R}_f)\mathbf{R}_s\mathbf{U}^m \end{aligned} \tag{6}$$

where $\mathbf{R}_f$ is a projection matrix, which extracts the displacement of a specific reference node from $\mathbf{U}_s$ and replicates this displacement across all surface degrees of freedom to match the original length of $\mathbf{U}_s$, enabling consistent matrix operations. $\mathbf{I}$ denotes an identity matrix. Although this correction leads to boundary forces that differ from those in the original macro model, it provides a more physiologically accurate representation of the internal stress and strain distributions within the VOI under in vivo conditions. These corrected mechanical states are essential for accurately simulating biological processes such as bone remodeling, mechano-regulated adaptation, and structural reinforcement. As demonstrated in previous studies [17,21,33–35], this approach enhances both the reliability and physiological relevance of the simulation outcomes.

2.3. Uncertainty error transfer from 'Macro Femur' model to 'Local VOI' model

It is widely acknowledged that loading conditions in the musculoskeletal system are subject to significant uncertainty due to individual variability in daily activities, pathological conditions, aging, and other individual factors [36,37]. Therefore, it is necessary to explore effective approaches to account for these uncertainties in bone geometry, mechanical loading, and structural analysis. In this work, the external load vector applied to the 'Macro Femur' model, denoted by $\mathbf{F}^m$, is no longer treated as a fixed deterministic quantity, but is instead modeled as a random variable $\tilde{\mathbf{F}}^m$ to better represent the stochastic nature of *in vivo* physiological loading. As such, it is expressed as follows:

$$\begin{aligned}\tilde{\mathbf{F}}^m &= \sum_{i=1}^{3}\tilde{\mathbf{F}}^{m,i} = \sum_{i=1}^{3}\tilde{A}_i\mathbf{F}^{m,i}, \quad \text{where } \mathbb{E}[\tilde{A}_i]=1\\ \bar{\mathbf{F}}^m &= \mathbb{E}[\tilde{\mathbf{F}}^m] = \sum_{i=1}^{3}\mathbb{E}[A_i]\mathbf{F}^{m,i} = \mathbf{F}^m\end{aligned} \tag{7}$$

where $\tilde{\mathbf{F}}^{m,i}$ represents the random external force vector associated with the ith musculoskeletal force group. In this study, we consider that $\tilde{\mathbf{F}}^{m,i}$ may vary in magnitude from its nominal (static) value, due to inherent uncertainties in physiological loading conditions. To capture this variation, each $\tilde{\mathbf{F}}^{m,i}$ is modeled as a product of a scalar random variable $\tilde{A}_i$ and its corresponding deterministic reference vector $\mathbf{F}^{m,i}$. The scaling factors $\tilde{A}_i$ are assumed to be statistically independent and have unit expectation, ensuring that the expected total force vector $\bar{\mathbf{F}}^m$ remains equal to the original deterministic force $\mathbf{F}^m$. This formulation preserves the physical fidelity of the loading conditions defined in [32], while incorporating realistic variability representative of actual physiological conditions.

By substituting the stochastic terms into the loading transfer equations for VOI FE model, namely Eqs. (4)–(6), the equivalent VOI surface displacement and loading vectors under uncertain musculoskeletal dynamics can be derived as:

$$\begin{aligned}\tilde{\mathbf{U}}_s &= (\mathbf{1}-\mathbf{R}_f)\mathbf{R}_s\tilde{\mathbf{U}}^m\\ \tilde{\mathbf{F}}_s &\approx (\mathbf{K}_{ss}-\mathbf{K}_{sl}\mathbf{K}_{ll}^{-1}\mathbf{K}_{ls})(\mathbf{I}-\mathbf{R}_f)\mathbf{R}_s\tilde{\mathbf{U}}^m\\ &= \sum_{i=1}^{3}\tilde{A}_i(\mathbf{K}_{ss}-\mathbf{K}_{sl}\mathbf{K}_{ll}^{-1}\mathbf{K}_{ls})(\mathbf{I}-\mathbf{R}_f)\mathbf{R}_s\mathbf{K}^{-1}\mathbf{F}^{m,i}\end{aligned} \tag{8}$$

where $\tilde{\mathbf{U}}_s$ and $\tilde{\mathbf{F}}_s$ denote the VOI surface displacement and loading vector, respectively. The above equation can be further simplified by expressing the boundary force vector $\tilde{\mathbf{F}}_s$ as a linear combination of three deterministic basis vectors $\mathbf{F}_s^i$, each scaled by a scalar random coefficient $\tilde{A}_i$ as follows:

$$\begin{aligned}\tilde{\mathbf{F}}_s &= \sum_{i=1}^{3}\tilde{A}_i\mathbf{F}_s^i\\ \mathbf{F}_s^i &= (\mathbf{K}_{ss}-\mathbf{K}_{sl}\mathbf{K}_{ll}^{-1}\mathbf{K}_{ls})(\mathbf{1}-\mathbf{R}_f)\mathbf{R}_s\mathbf{K}^{-1}\mathbf{F}^{m,i},\end{aligned} \tag{9}$$

This formulation enables effective propagation of input uncertainties from musculoskeletal dynamics to the boundary conditions of the VOI FE model, using only three independent random variables $\tilde{A}_i$ and a set of precomputed deterministic vectors $\mathbf{F}_s^i$. Overall, this approach not only accounts for gait-induced uncertainties but also removes rigid-body motion components from the displacement field—an improvement over conventional boundary load estimation methods such as those discussed in [31]. As a result, the proposed method provides a more physically meaningful and numerically stable boundary condition for the VOI model, enhancing both the convergence and physiological fidelity of the subsequent simulations.

2.4. Patient-specific trabecular bone reconstruction

Trabecular bone continuously remodels in response to mechanical stimuli, gradually aligning its structure along principal stress directions and increasing trabecular thickness to enhance load-bearing capacity [38]. Interestingly, this biological adaptation process bears a strong resemblance to structural topology optimization. As highlighted in [18], bone remodeling – often modeled using strain energy density (SED) as the regulatory stimulus – is conceptually and algorithmically aligned with the mathematical framework of compliance-based topology optimization. Notably, SED-driven bone remodeling algorithms have been shown to produce structural patterns remarkably similar to those generated through topology optimization across a variety of scenarios [18]. Furthermore, the relationship between bone density and stiffness follows a power-law formulation that closely mirrors the SIMP (Solid Isotropic Material with Penalization) model commonly used in topology optimization [19,39]. These analogies support the interpretation of bone as a self-optimizing system and provide a rigorous foundation for using topology optimization to reconstruct trabecular bone microarchitecture.

In this study, we employ a robust topology optimization (RTO) framework that incorporates uncertainties arising from biological variability, such as individual differences in gait patterns and daily activity levels. Unlike conventional compliance-based formulations that seek the stiffest structure under fixed loads, our approach aims to obtain a mechanically-reliable and biologically-reasonable structure that remains effective under a range of physiological conditions. This shift in objective better reflects how real trabecular bone adapts—not by achieving extreme stiffness, but by maintaining sufficient structural integrity across diverse mechanical demands, as illustrated in Fig. 1(c). The proposed RTO strategy prioritizes consistency of structural stiffness under a range of musculoskeletal forces, aligning more closely with the inherently robust nature of bone remodeling. Building upon this bio-mechanically motivated perspective, we establish the following optimization framework to guide the reconstruction of trabecular architecture under uncertain loading conditions:

$$\begin{aligned}\min_{\rho_e}\quad & C_t = w_1\cdot\bar{C}+w_2\cdot\sigma_C^2\\ s.t.\quad & g_1(\boldsymbol{\rho}) = \|V_j^{(k)}(\rho_i)-V_{j,o}^{(k)}\|_{p_1}\\ & \qquad = \left(\sum_{j=1}^{N_j}\left|V_j^{(k)}(\rho_i)-V_{j,o}^{(k)}\right|^{p_1}\right)^{\frac{1}{p_1}} \le \varepsilon_1\\ & g_2(\boldsymbol{\rho}) = \frac{1}{N}\sum_{i}^{N}(\rho_i-0.9)(0.05-\rho_i)\le 0\end{aligned} \tag{10}$$

where C_t denotes the total objective function consisting of the expected structural compliance $\bar{C}$ and its variance σ_C^2. The weights w_1 and w_2 control the trade-off between optimal stiffness and robustness. This formulation enables the optimization process to account for the variability in external forces while maintaining a stable mechanical response. In this work, $w_1 = 1$ and $w_2 = 0.5$ are selected via systematic parametric testing based on the baseline topology optimization solution. With these values, the objective ratio between mean compliance terms and variance terms almost falls within a practical range of about 5:1 to 10:1 for all cases.

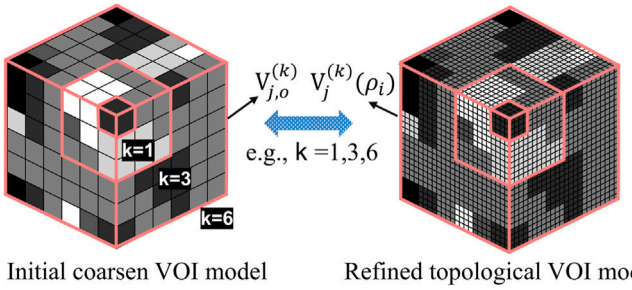

Fig. 2. The demonstration of local volume fraction constraint g_1 in the bone reconstruction computation. In this way, the volume difference between initial CT VOI model block ($V_{k,o}$) and refined VOI model block ($V_k(\rho_i)$) at level k is limited during the optimization.

To ensure anatomical plausibility and numerical stability, several constraints are integrated into the optimization process. The volume constraint $g_1(\rho)$ enforces consistency between the optimized and reference density distributions. Specifically, the average relative density $V_j^{(k)}(\rho)$ in each block region must remain close to the reference value $V_{j,o}^{(k)}$, extracted from the original low-resolution CT data, as illustrated in Fig. 2. Herein, k indicates the subdivision level, and N_j is the number of block regions in the VOI model. This constraint preserves patient-specific bone distribution characteristics. It is implemented using a global p-norm aggregation with $p_1 = 16$ and a tolerance threshold $\epsilon_1 = 0.01$, reflecting the typical 1% error margin in clinical CT acquisition. Additionally, a penalization term $g_2(\rho)$ is introduced to promote the convergence of the optimization process, towards realistic bone material distribution. Herein, N denotes the total number of the elements in the refined topological VOI model, as illustrated in Fig. 2.

The robust topology optimization (RTO)-based trabecular reconstruction process is implemented in MATLAB (version 2023b), utilizing the Method of Moving Asymptotes (MMA) as the optimization solver, following the framework in [40]. In particular, the sensitivities of the objective and constraint functions are calculated analytically. For brevity, we denote the random variables $\tilde{A}_i$ in Eq. (9) as A_i throughout the following derivations, unless otherwise specified. The compliance of the VOI FE model can be expressed as a second-order function with respect to the random variables:

$$\begin{aligned} C &= \left(\sum_{i=1}^{3} A_i \mathbf{F}^i\right)^T \mathbf{K}^{-1} \left(\sum_{j=1}^{3} A_j \mathbf{F}^j\right) \\ &= \sum_{i=1}^{3}\sum_{j=1}^{3} A_i A_j \cdot (\mathbf{F}^i)^T \mathbf{K}^{-1} \mathbf{F}^j \\ &= \sum_{i=1}^{3}\sum_{j=1}^{3} A_i A_j c_{ij}, \quad \text{with } c_{ij} = (\mathbf{F}^i)^T \mathbf{K}^{-1} \mathbf{F}^j \end{aligned} \tag{11}$$

Accordingly, considering A_i are independent from each other and each of its expected value $\mathbb{E}(A_i) = 1$, the expectation of the objective and sensitivity can be expressed as:

$$\begin{aligned} \bar{C} &= \mathbb{E}(C) = \sum_{i,j}^{3} \mathbb{E}[A_i A_j] c_{ij} = \mathbf{F}^T \mathbf{U} = \mathbf{U}^T \mathbf{K} \mathbf{U}, \\ \frac{\partial \bar{C}}{\partial \boldsymbol{\rho}} &= -\mathbf{U}^T \frac{\partial \mathbf{K}}{\partial \boldsymbol{\rho}} \mathbf{U} \end{aligned} \tag{12}$$

where $\mathbf{U}$, $\mathbf{F}$ and $\mathbf{K}$ represent the global displacement vector, external force, and stiffness matrix of the VOI model under standard deterministic loading, as given by Eq. (3) in Section 2.2.

Following the Solid Isotropic Material with Penalization (SIMP) method [39,40], the above expressions can be reformulated in terms of element-wise forms. For clarity, we denote the element index by e, replacing i in Eq. (10) in the following formulas. Accordingly, for the eth element, we have:

$$\begin{aligned} \mathbf{k}_e &= E_0 \rho_e^3 \mathbf{k}_0, \\ \frac{\partial \bar{C}}{\partial \rho_e} &= -\mathbf{u}_e^T \frac{\partial \mathbf{k}_e}{\partial \rho_e} \mathbf{u}_e = -3 E_0 \rho_e^2 \mathbf{u}_e^T \mathbf{k}_0 \mathbf{u}_e \end{aligned} \tag{13}$$

where E_0 is the Young's modulus of compact bone. $\mathbf{k}_0$ represents the reference elemental stiffness matrix and constitutive matrix with unit modulus $E = 1$, respectively [40]. $\mathbf{k}_e$ and $\mathbf{u}_e$ denoted elemental stiffness matrix and elemental displacement vector. On the other hand, the variance term of the compliance, σ_C^2 is formulated using the full fourth-order function expansion of coefficients A_i, as follows:

$$\begin{aligned} \sigma_C^2 &= \mathbb{E}[\tilde{C}^2] - (\bar{C})^2 \\ &= \sum_{i,j,k,l} \mathbb{E}[A_i A_j A_k A_l] \cdot c_{ij} c_{kl} - \left(\sum_{i,j} \mathbb{E}[A_i A_j] \cdot c_{ij}\right)^2 \\ &= \sum_{i,j,k,l} \left(\mathbb{E}[A_i A_j A_k A_l] - \mathbb{E}[A_i A_j]\mathbb{E}[A_k A_l]\right) \cdot c_{ij} c_{kl} \end{aligned} \tag{14}$$

This formulation enables precise propagation of gait-induced uncertainty in cases with a small number of independent musculoskeletal force components. Furthermore, it can be simplified as:

$$\begin{aligned} \sigma_C^2 = &\sum_{i=1}^{3} \left(\mu_4^{(i)} - \left(\sigma_i^2\right)^2\right) \cdot c_{ii}^2 \\ &+ \sum_{\substack{i,j=1 \\ i \neq j}}^{3} \left[\left(\sigma_i^2 \sigma_j^2 + \sigma_i^2 + \sigma_j^2\right)\left(c_{ij}^2 + c_{ii} c_{jj}\right) + \mu_3^{(i)} \cdot c_{ii} c_{ij}\right] \\ &+ \sum_{\substack{i,k,l=1 \\ \text{all distinct}}}^{3} \sigma_i^2 \cdot c_{ii} c_{kl} \end{aligned} \tag{15}$$

where σ_i^2 is the variance of the A_i. $\mu_3^{(i)}$, $\mu_4^{(i)}$ are the third- and forth-order central moments of the independent random variable A_i. In particular, for a uniform distribution $A_i \sim \mathcal{U}[a_i, b_i]$ as used in this work, we have:

$$\mu_3^{(i)} = 0, \quad \mu_4^{(i)} = \frac{(b_i - a_i)^4}{80} \tag{16}$$

Regarding the sensitivities of the variation term with respect to ρ_e, it can be expressed using Einstein summation notation:

$$\begin{aligned} \frac{\partial\, \sigma_C^2}{\partial\, \rho_e} = &\sum_{i=1}^{3} 2\left(\mu_4^{(i)} - \sigma_i^4\right) \cdot c_{ii} \frac{\partial c_{ii}}{\partial \rho_e} \\ &+ \sum_{\substack{i,j=1 \\ i \neq j}}^{3} 2\left(\sigma_i^2 \sigma_j^2 + \sigma_i^2 + \sigma_j^2\right) \cdot c_{ij} \frac{\partial c_{ij}}{\partial \rho_e} \\ &+ \sum_{\substack{i,j=1 \\ i \neq j}}^{3} \left(\sigma_i^2 \sigma_j^2 + \sigma_i^2 + \sigma_j^2\right) \cdot \left(\frac{\partial c_{ii}}{\partial \rho_e} c_{jj} + c_{ii} \frac{\partial c_{jj}}{\partial \rho_e}\right) \\ &+ \sum_{\substack{i,j=1 \\ i \neq j}}^{3} \mu_3^{(i)} \cdot \left(\frac{\partial c_{ii}}{\partial \rho_e} c_{ij} + c_{ii} \frac{\partial c_{ij}}{\partial \rho_e}\right) \\ &+ \sum_{\substack{i,k,l=1 \\ \text{all distinct}}}^{3} \sigma_i^2 \cdot \left(\frac{\partial c_{ii}}{\partial \rho_e} c_{kl} + c_{ii} \frac{\partial c_{kl}}{\partial \rho_e}\right) \end{aligned} \tag{17}$$

where the sensitivity of the compliance sub-term c_{ij} with respect to the design variable ρ_e is computed as:

$$\frac{\partial c_{ij}}{\partial \rho_e} = -(\mathbf{u}_e^i)^T \frac{\partial \mathbf{k}_e}{\partial \rho_e} \mathbf{u}_e^j,$$

where $\mathbf{u}_e^i$ denotes the element-wise displacement vector at element e, extracted from the global displacement solution field $\mathbf{U}^i = \mathbf{K}^{-1}\mathbf{F}^i$ under the ith individual loading case. Based on above, the final gradient information need for objective problem in Eq. (10) can be calculated

as follow:

$$C_t = w_1 \cdot \bar{C} + w_2 \cdot \sigma_C^2$$
$$\frac{dC_t}{d\rho_e} = w_1 \frac{\partial \bar{C}}{\partial \rho_e} + w_2 \frac{\partial \sigma_C^2}{\partial \rho_e} \tag{18}$$

Finally, the sensitivities of the constraint functions are expressed as:

$$\frac{\partial g_1}{\partial \rho_e} = \sum_{j=1}^{N_k} \frac{1}{N_k} \left(V_j^{(k)} - V_{j,o}^{(k)} \right)^{p_1 - 1} \cdot (g_1)^{1-p_1}$$
$$\frac{\partial g_2}{\partial \rho_e} = \frac{1}{N} \left(-2\rho_e + 0.95 \right) \tag{19}$$

where N_k is the total scalar number of block regions in the whole VOI domain with respect to k level. Based on above, the corresponding gradient optimization procedure can be completed to reconstructed the final bone geometry.

Statistical analysis was performed to evaluate differences in primary trabecular morphometric parameters, including bone volume fraction ($\frac{BV}{TV}$), trabecular thickness (*Tb.Th*), trabecular number ($Tb.N$), and trabecular spacing (*Tb.Sp*). Multivariate analysis of variance (MANOVA) was applied to assess overall differences among the five individual samples and between the conventional topology optimization (TO) and the proposed robust topology optimization (RTO) methods, respectively. Subsequent uni-variate comparisons were conducted using paired t-tests to identify significant differences in individual parameters. Additional structural metrics, including connectivity density (Conn.D), degree of anisotropy (DA), and structure model index (SMI), were analyzed for completeness and included in Appendix for supplementary reference. All statistical procedures were implemented in Origin (OriginLab Corporation, Northampton, USA). A significance level of $p < 0.05$ was adopted for all statistical evaluations.

3. Results

To demonstrate the effectiveness of the proposed method, two examples are firstly studied in this section: one is based on a rabbit femur and the other is based on a human femur.

3.1. Rabbit femur example

To verify the proposed method, we first applied the RTO-based computational framework to reconstruct high-resolution trabecular structures of a rabbit femur. Since only high-resolution CT scans of the rabbit femur were available, we artificially generated low-resolution (LR) images from those HR CT scans through a numerical process, which applies an averaging and blurring method combined with additional random perturbations.

To further validate the proposed method, we processed the artificially generated low-resolution images using the RTO-based computational framework, with minor parameter adjustments to account for anatomical and biomechanical differences between rabbits and humans. Notably, rabbits exhibit a jumping-dominant locomotion pattern, resulting in different loading modes compared to humans. Accordingly, two compressive forces were applied as macro-level loading conditions in the finite element model, targeting the femoral head and the greater trochanter regions. These forces were aligned with the femoral neck axis, as described in [41]. Based on typical jumping mechanics, the force magnitudes were set to 240% and 60% of a standard rabbit body weight (3.2 kg) for the femoral head and trochanter, respectively. To account for variability and enhance robustness, the force amplitudes were perturbed using uniform random distributions: $A_1 \sim \mathcal{U}[0.8, 1.2]$ and $A_2 \sim \mathcal{U}[0.9, 1.1]$ for the femoral head and the trochanter, respectively.

The VOI model for this rabbit femur sample was defined as a cube with a side length of 10.8 mm. The mesh resolution was refined from an initial element size of 0.9 mm to 0.225 mm, matching the resolution of the standard high-resolution CT scans. For the CT-based volume constraint g_1, we applied two scale levels: $k = 1.8$ mm and $k = 10.8$ mm, with a threshold of $\epsilon_1 = 2\%$. Although the original CT resolution is 0.9 mm, using a slightly relaxed constraint at 1.8 mm, preventing convergence issues during optimization. In addition, the larger scale $k = 10.8$ mm serves as a global constraint to regulate the overall volume distribution.

The imaging workflow and final reconstruction results are shown in Fig. 3. Fig. 3(a) presents the original CT scan of the rabbit femur, with the volume of interest (VOI) highlighted in the femoral head region. Figs. 3(b) and 3(c) display the artificially generated LR image and the original HR CT scan within the VOI, respectively. Fig. 3(d) shows the 3D reconstruction of the trabecular bone structures within the VOI, and Fig. 3(e) provides a sectional view extracted from this 3D model. As illustrated in Fig. 3(f), the reconstructed model successfully captures key internal features – such as cavities located in the upper-left and lower-central regions – with strong spatial agreement to the HR CT data. Quantitative evaluations further confirm the reconstruction accuracy. The global bone volume fraction (BV/TV) in the reconstructed VOI is 39.5%, closely matching the 39.0% obtained from the HR CT, with a relative error of less than 2%. The reconstructed trabecular thickness (*Tb.Th*) and trabecular spacing (*Tb.Sp*) are 0.121 mm and 0.175 mm, respectively, compared to 0.118 mm and 0.199 mm in the HR CT, indicating high morphological consistency. Additionally, the feature similarity index (FSIM) [42] between the reconstructed VOI and the HR CT reaches 0.94 (FSIM = 1 denotes perfect similarity). These results demonstrate that the proposed method can reliably reproduce trabecular microstructures with high fidelity. This provides preliminary validation of the computational framework and highlights its potential for future applications in clinical diagnosis and decision support.

3.2. Human-being femur example

Given that the typical trabecular thickness in the human femur is approximately 0.2 mm [43,44], a model resolution of around 0.05 mm is recommended to accurately replicate the intricate trabecular geometry. However, such ultra-high-resolution CT data at that scale were not available for this study. Instead, we selected a zoomed-in volume of interest (VOI), where higher-resolution bone mineral density patterns are reconstructed from lower-resolution input data. In this context, the accuracy of the proposed RTO-based bone reconstruction method relies primarily on the relative refinement between the original and target element sizes, and is independent from the absolute resolution of the CT scans.

To this end, a $24 \times 24 \times 24\,\text{mm}^3$ volume of interest (VOI) was segmented from low-resolution (LR) CT images and used for the construction. In detail, the work selects femur head region with distinct characteristics for the effective verification, as shown in Fig. 4(a). The mesh resolution was refined from 1.2 mm to 0.3 mm, representing a transition from LR data to a higher-resolution reconstruction. As in the rabbit femur case, two scale levels were used for the volume constraint g_1: $k = 2.4$ mm and $k = 24$ mm, respectively. Boundary conditions were applied following the settings described in Section 2, where three typical musculoskeletal force groups shown in Fig. 1 are set in the macro proximal femur model. The distal side of the femur bone are clamped in all directions. In addition, regrading the robustness of external loading, the hip contact force $\mathbf{F}^{m,1}$ and abductor force $\mathbf{F}^{m,2}$ were assigned uniform random amplitudes $\mathcal{U}[0.8, 1.2]$. The vastus lateralis force $\mathbf{F}^{m,3}$, which is generally subject to greater variability, was modeled using a broader distribution $\mathcal{U}[0.6, 1.4]$ in this work [45,46]. The final reconstruction result is presented in Fig. 4. Fig. 4(b) and (c) suggest the low resolution CT and high resolution CT corresponding the VOI region in the initial CT scanning (Fig. 4(a)). Fig. 4(d) and (e) are the reconstructed 3D VOI model and corresponding centering sectional face. Fig. 4(f) suggest the direct geometry comparison for real high resolution CT and predicted image. The comparison image

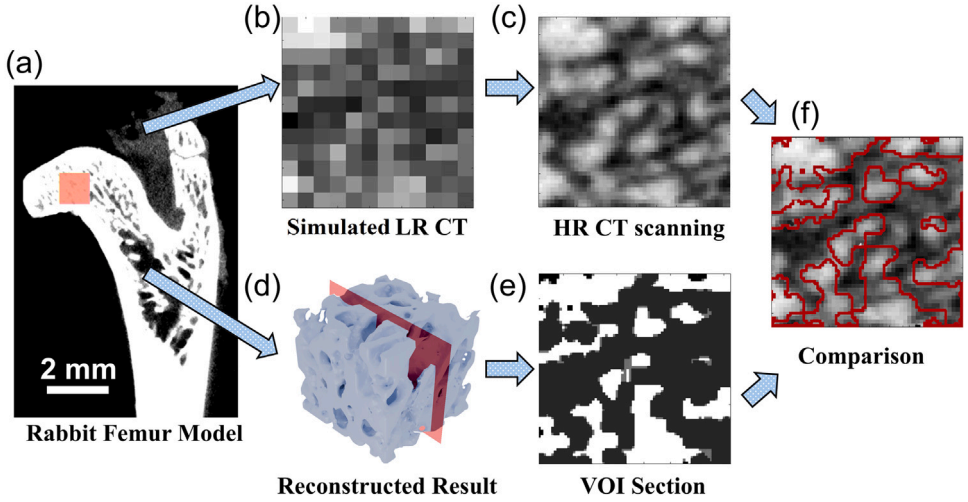

Fig. 3. Bone reconstruction verification for the rabbit femur. (a) Typical rabbit femur model with VOI region. (b) and (c) are the corresponding low resolution and high resolution CT scanning for the VOI region. (d) and (e) are corresponding reconstructed result and high resolution middle plane section. (f) is the comparison view of image (c) matrix and image (e) boundary edges.

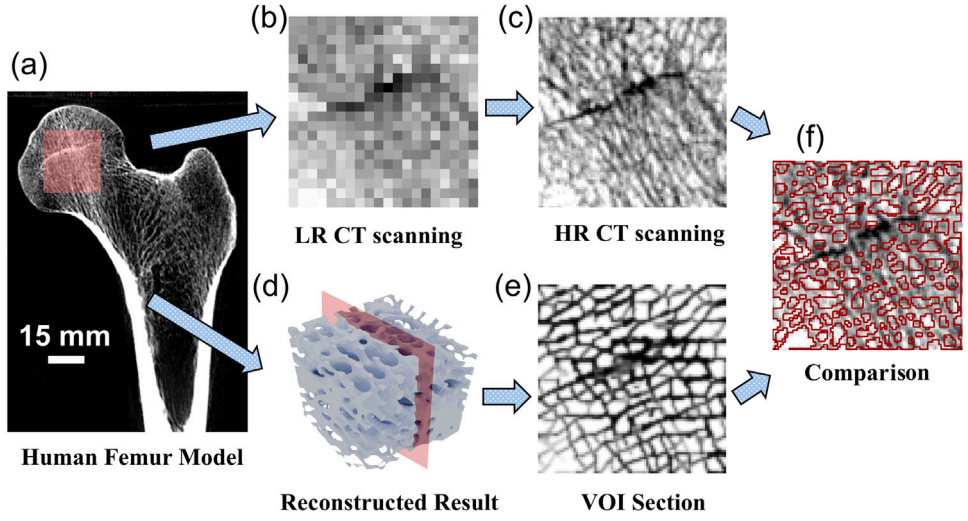

Fig. 4. Bone reconstruction verification for the Zoomed human-being femur VOI region. (a) Typical femur model with VOI region. (b) and (c) are the corresponding low resolution and high resolution CT scanning for the femur region. (d) and (e) are the reconstructed result and corresponding, high resolution middle plane section. (f) is the comparison view of image (c) matrix and image (e) boundary edges.

in Fig. 4(f) highlights local consistencies in key structural regions, such as the blank area in the bottom-left corner, the dense arc of principal tensile trabecular in the mid-region, and the upper-right region [47]. Under the influence of compliance performance and local volume constraints by LR CT, the predicted image can not only construct bone network along the diagonal hip contact force direction (following macro mechanic regularity), but also keeps patient-specific spares or pores features under individual error. The feature similarity index (FSIM) between the reconstructed model and the HR CT image reaches approximately 0.94, which further approves the method's accuracy and robustness.

3.3. Human femoral VOI reconstruction

In this section, age 50 ~ 65 femur bone samples through air-drying method [48] of 6 × 6 × 6 mm^3 VOIs located at the femoral head, as illustrated in Fig. 4, are reconstructed using the proposed method. The VOI is still selected at femoral head, while its pixel size is refined from an initial element size of 0.3 mm to 0.06 mm, enabling sufficient resolution for capturing trabecular branching patterns. Accordingly, the mesh resolution increases from 20 × 20 × 20 to 100 × 100 × 100. To avoid high computational efficiency, only a 0.6 mm thick middle layer is designated as the active region during optimization, while the surrounding layers are treated as topological passive elements in the optimization-based reconstruction process [40]. This setup can adequately reconstruct the detailed trabecular architecture for clinical evaluation, while greatly reducing computational time from 3 days to less 20 min per case (300 iterations) on a Dell workstation (AMD Ryzen 7980X CPU, 128 GB RAM, A4000 16 GB GPU).

Fig. 5 compares the reconstructed trabecular structures obtained from conventional topology optimization (TO) and the proposed robust topology optimization (RTO) method. The TO results are generated by setting the objective weight $w_2 = 0$. While both approaches qualitatively align with the low-resolution CT (LR-CT) data, the RTO method yields structures with notably improved connectivity and branching of the trabecular network. This enhancement is particularly evident in Case-5, where RTO produces slender, well-connected trabecular struts with a more homogeneous spatial distribution, in contrast to the local voids seen in the TO results.

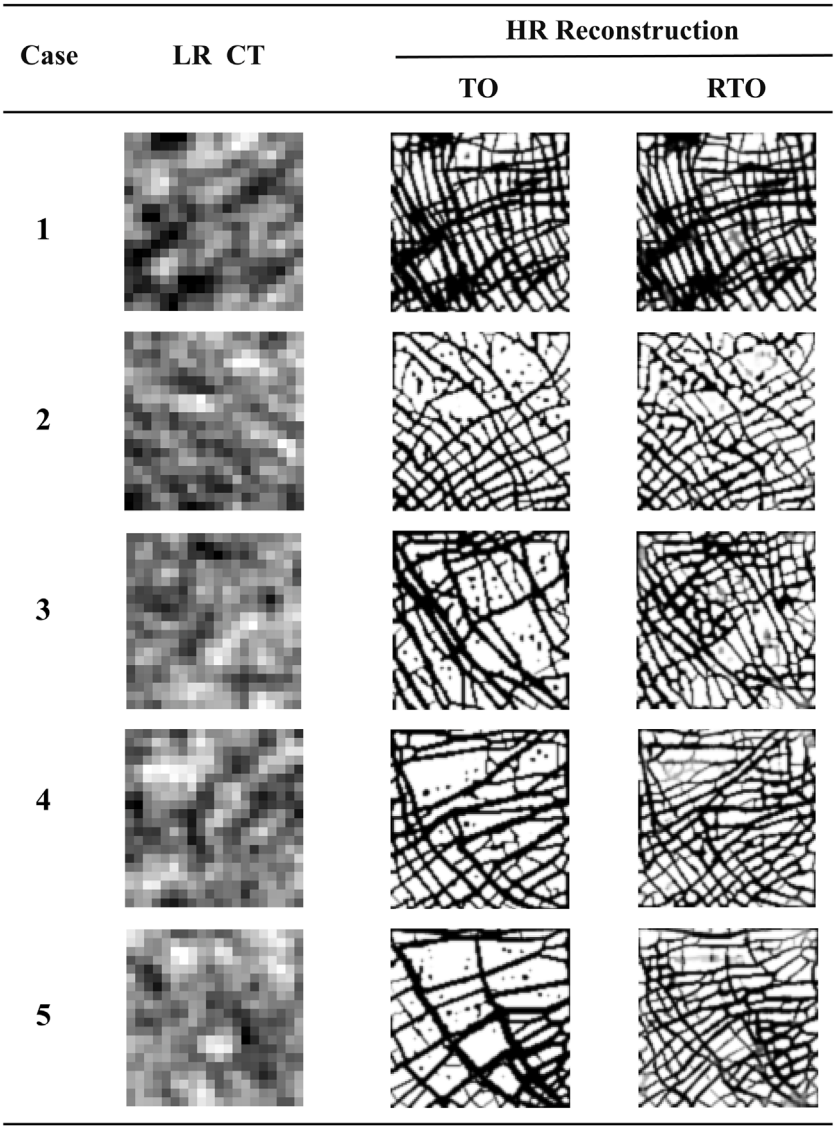

Fig. 5. The bone reconstruction solutions for 5 standard femoral head VOIs based on 0.3 mm initial resolution, by either topology or robust topology optimization method.

Conventional topology optimization (TO) methods typically do not generate isolated elements, as they contribute the material mass but have no influence on the stiffness performance. However, in the context of trabecular bone reconstruction, such as in this study and in [14], the enforcement of local volume constraints (g_1) can lead to the appearance of isolated pixels in void regions, as observed in most TO results in Fig. 5. These isolated bone fragments not only reduce the visual quality of the reconstructed image but also lack anatomical plausibility, given that suspended bone mass within the marrow is unrealistic. In contrast, the proposed RTO-based bone reconstruction method integrates these dense regions into the surrounding trabecular network, promoting branching along multiple principal stress trajectories. This leads to significantly improved directional connectivity and structural realism, offering clear advantages for both biomechanical accuracy and image-based bone structure modeling.

Correspondingly, the average FSIM index for the TO and RTO predictions with respect to LR images are of 92.4% and 93.6%, evidencing the overall structural feature similarity for the both predicted images compared to initial coarsen CT structure; Typically for Case-5, the FSIM is measured to be improved from 91.2% to 93.4% by robust technique consideration. From engineering perspective, above data reveals the reinforce isotropic elasticity of the RTO structure by lower the error influence, suggesting enhanced mechanical performance of structure by facilitating stress transfer across multiple directions, thus improving the stability of the structure under variable loading conditions [29,49]. Although the FSIM index indicates a high degree of visual similarity in the overall alignment of the trabecular networks produced by both TO and RTO, it does not fully capture the statistical differences in their trabecular properties. To quantitatively assess these differences – especially those relevant to clinical diagnosis – four key trabecular parameters were extracted using ImageJ (ver. 1.53): bone volume fraction (BV/TV), trabecular thickness ($Tb.Th$), trabecular number ($Tb.N$), and trabecular spacing ($Tb.Sp$). These standard bone quality metrics are summarized in Table 1. Additionally, Fig. 6 presents error bar plots showing the mean values and ranges across five representative cases for both TO and RTO results. More detailed FEM verifications for mechanical performance of the optimal solutions are provided in the Appendix C.

From the perspective of these 5 different samples, the proposed RTO method maintains the patient-specific characteristics of trabecular

Table 1
The corresponding trabecular parameters, i.e. bone/total volume fraction, trabecular thickness, number and spacing, of the five bone reconstructed cases.

Case	BV/TV (%)		Tb.Th (mm)		Tb.N (mm^{-1})		Tb.Sp (mm)	
	TO	RTO	TO	RTO	TO	RTO	TO	RTO
1	41.333	38.203	0.155	0.193	1.581	1.527	0.483	0.505
2	62.197	55.366	0.058	0.083	1.632	1.701	0.463	0.438
3	53.682	49.809	0.104	0.102	1.388	1.685	0.57	0.443
4	53.584	49.252	0.101	0.096	1.686	1.792	0.443	0.408
5	54.477	45.299	0.134	0.118	1.152	1.760	0.718	0.418

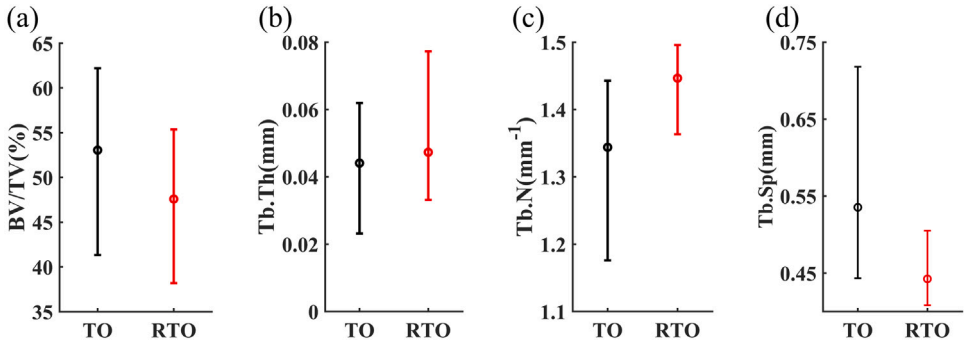

Fig. 6. The statistical comparison of five bone reconstruction cases for bone/total volume fraction, trabecular thickness, number and spacing. The error bar plot showing the mean values as the central markers, with the upper and lower limits representing the range of variation.

Fig. A.1. Five femur bone samples used in the work.

structures across different samples, despite incorporating robustness into the optimization. A multivariate analysis of variance (MANOVA) confirms that sample identity significantly influences the combined set of trabecular parameters (Wilks' $\lambda < 0.001$, $F_{4,1} > 1000$, $p < 0.001$), providing statistical evidence for the distinctiveness and individuality of the five reconstructed volumes of interest (VOIs).

From a methodological perspective, multivariate analysis of variance (MANOVA) further identified a significant overall difference between the conventional TO and proposed RTO methods across the full set of trabecular parameters (Wilks' $\lambda = 0.015$, $F_{4,1} = 112$, $p = 0.0043$). Consistently, paired t-tests reveal notable differences in key trabecular parameters, particularly in bone volume fraction ($\frac{BV}{TV}$, $p = 0.008$) and trabecular number ($Tb.N$, $p \approx 1.5 \times 10^{-5}$). The trabecular thickness ($Tb.Th$, $p = 0.472$) and spacing ($Tb.Sp$, $p = 0.179$) do not show statistically significant differences likely due to the limited sample size ($n < 5$). Despite, a large absolute error at $\tilde{0}.03$ mm level is still observed in Sample 2, corresponding approximately 12.5% of the standard trabecular thickness 0.2 mm [44]. These results clearly demonstrate significant differences between the conventional TO and the proposed RTO computations, supporting the effectiveness of the newly developed method. Besides, in line with the observations discussed in Fig. 5, the RTO results also demonstrate a marked reduction in variability. For instance, the standard deviation of $Tb.Sp$ in the RTO group is reduced by 66% compared to the TO group.

These improvements in consistency are further illustrated by the narrower error bars shown in Fig. 6. For the RTO method, the corresponding range of the terms, especially $Tb.N$ and $Tb.Sp$ are obviously smaller than that of the existing TO methods. This can be explained by the error elimination effect of RTO method, which greatly decreases the influence of diverse error, e.g., machine detect, patient body, and surgeons operation through the robust sensitivity mechanism.

In overview, the above findings indicate that the RTO method not only preserves patient-specific morphological features but also produces more accurate trabecular micro-architectures relevant for clinical diagnosis. While TO reconstructions exhibit large and unpredictable variability across different cases, RTO consistently delivers more controlled and clinically interpretable outcomes. For clarity, we mainly focus on the primary trabecular geometric parameters i.e., $BV/TV, Tb.Th, Tb.N, Tb.Sp$ in this section, while other supplementary structural parameters including connectivity density ($Conn.D$), degree of anisotropy (DA), and structure model index (SMI), also exhibit consistent and favorable trends in the proposed RTO framework. Further details regarding these parameters please refer to Appendix B.

4. Discussion

Many conventional image processing methods aim for absolute clarity in their outputs, often producing binary (0–1) representations of structures such as bone tissue. This thresholding strategy assumes sharply defined material boundaries, which simplifies segmentation but fails to capture the physiological complexity of trabecular bone. In reality, trabecular bone exhibits continuous, gradient-density distributions.

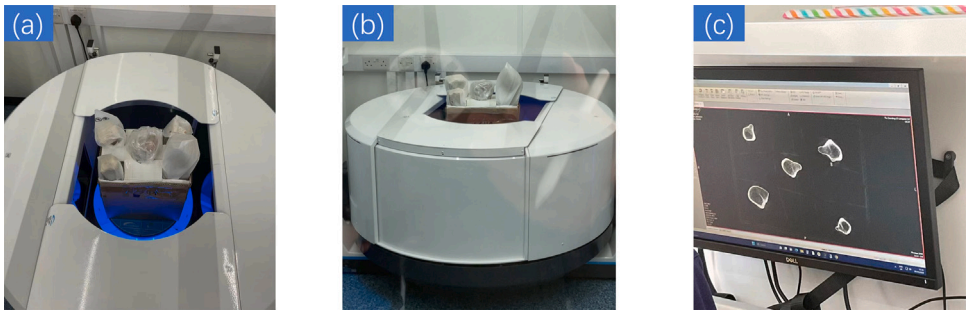

Fig. A.2. CT scan image machine and scanning process.

In this study, intermediate-density elements (i.e., grayscale units) are retained throughout the optimization process. This modeling choice provides two key advantages. First, it better reflects the biological nature of trabecular bone, where even seemingly solid regions are composed of porous, multi-scale substructures such as osteons and Haversian canals. Second, it improves algorithmic flexibility, enabling the model to better accommodate complex imaging constraints and supporting more stable convergence during the reconstruction of intricate bone morphologies.

Beyond the use of grayscale density values, the proposed method also represents a conceptual and practical departure from both traditional clinical image processing techniques and contemporary data-driven models. Unlike machine learning-based approaches that rely on large training datasets and external supervision, our method is fully grounded in mechanical principles and biological rules—most notably Wolff's law, which governs bone remodeling in response to mechanical loading. This biologically-informed framework is not only data-independent and computationally efficient, but also highly interpretable, making it particularly well-suited for lightweight, low-cost clinical applications such as plugin software for diagnostic imaging.

Compared to previous TO-based studies [14,21,50], the RTO-based approach introduces a novel interpretation of Wolff's law that accounts for biological uncertainty. Traditional TO methods often equate Wolff's law with maximizing structural stiffness under muscle loading. This view is relatively static and engineering-centric. It neglects the multi-functional requirements of biological tissue, such as adaptability, energy absorption, and robustness under varying loads. Our method incorporates robustness directly into the optimization process and emphasizes structural stability in response to load variation. We offer a biomechanically grounded reinterpretation of Wolff's law as a balance between acceptable stiffness and enhanced load-bearing stability that more closely aligns with the natural behavior of bone. The improved accuracy of RTO-based reconstructions compared with conventional TO supports this revised understanding. Minimizing compliance variance serves as a mechanically rigorous proxy for biological robustness supported by both computational simulations and experimental evidence. Bone adaptation prioritizes stable mechanical performance under variable physiological loads rather than optimal stiffness under a single load condition [19,21]. Reduced variability in trabecular mechanical response is directly linked to enhanced structural stability, fracture resistance, and lower heterogeneity in experimental tests and micro-finite element studies [51–53]. Our definition of robustness aligns with the physiological need for consistent load-bearing behavior under real-world loading uncertainty.

The VOI sizes in this work for rabbit and human femurs were determined based on CT voxel resolution, trabecular representativeness, and computational feasibility. For rabbit femurs (0.225 mm voxel size) and standard human femurs (0.6 mm voxel size), we used VOI side lengths of 10.8 mm (48 × 48×48 FE grid) and 24 mm (40 × 40×40 FE grid), respectively, to ensure consistent structural representation across species. For high-resolution femoral head trabecular reconstruction, a 6 mm cubic VOI with a 100 × 100×100 discretization (0.06 mm unit length) was adopted to accurately resolve fine trabecular morphology (0.2 mm thickness [44]) while maintaining computational efficiency. Overall, all VOI dimensions were selected to balance microstructural fidelity, statistical representativeness, and numerical tractability, with the proposed RTO framework remaining scalable to larger domains given additional computational resources.

Table B.2
Structural parameters ($Conn.D, DA, SMI$) for each sample by TO and RTO reconstruction.

Sample	Method	Conn.D ($1/mm^3$)	DA	SMI
1	TO	0.152	1.56	2.06
1	RTO	0.145	1.50	2.01
2	TO	0.171	1.63	2.15
2	RTO	0.163	1.57	2.10
3	TO	0.148	1.54	2.00
3	RTO	0.141	1.49	1.96
4	TO	0.165	1.60	2.08
4	RTO	0.157	1.54	2.03
5	TO	0.163	1.59	2.05
5	RTO	0.155	1.53	2.00

The assumption of statistically independent scaling factors A_i is a practical and well-supported simplification for robust topology optimization, justified by the distinct anatomical origins and relatively low physiological correlation among the three hip load components [32,46]. This treatment greatly improves computational feasibility for uncertainty propagation and moment expansion, while only slightly and conservatively overestimating load variability [36]. The ranges $A_1 \sim U[0.8, 1.2]$, $A_2 \sim U[0.8, 1.2]$, and $A_3 \sim U[0.6, 1.4]$ are rigorously based on in vivo hip load measurements and musculoskeletal uncertainty studies, with uniform distributions selected to avoid subjective bias and maintain numerical efficiency [36,45,46].

High-resolution trabecular reconstruction involves heavily constrained optimization that can pose convergence challenges. To address this issue, the regularization term g_2 is introduced to stabilize the MMA solution and improve efficiency, while the SIMP penalty factor 3 is used to promote binary convergence. Both parameters are selected to balance numerical performance and physical consistency. With these settings, the RTO framework converges reliably within 300 ± 50 iterations, and g_2 reduces the total number of iterations by approximately 33%. Numerical tests confirm that the initial density field affects convergence speed but has negligible influence on the final architecture, indicating stable and robust optimization performance.

In summary, the proposed mechanically driven and biologically informed framework offers a new perspective for clinical image processing that explicitly incorporates biological loading uncertainty. It delivers interpretable results, aligns with established biomechanical principles, and scales efficiently for both research and clinical use. Meanwhile, several limitations also point to opportunities for further strengthening the approach. First, the current uncertainty setting is based on perturbations of a small set of representative load components under simplified assumptions; incorporating rich time-varying patterns

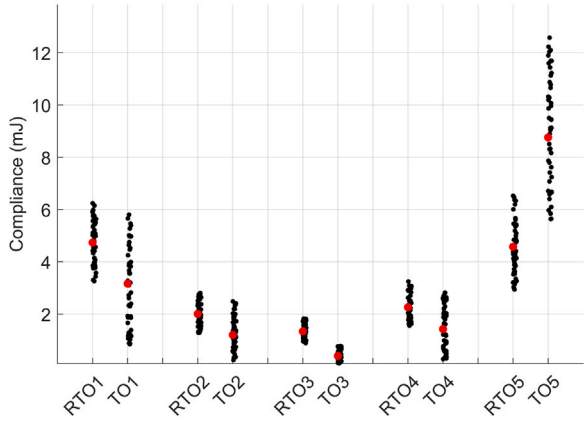

Fig. C.1. Performance comparison between RTO and TO reconstruction models for five human femur samples. Red points represent the expected compliance values, while black points denote individual compliance results from 50 random perturbed load cases.

and rare events would broaden its coverage of real-world loading. Second, reconstruction is performed on selected VOIs with boundary conditions transferred from a macro-scale femur model, and further refinement of the load-transfer procedure and macro–micro scale consistency is expected to improve local fidelity. Third, the present validation focuses on healthy and single anatomical coverage; extending the study to larger datasets and additional regions (e.g., osteoporosis sample, femoral neck and intertrochanteric area) will be beneficial to consolidate generalizability for proposed method.

5. Conclusions

In this work, we propose a novel, lightweight, biomechanics-driven image processing method for reconstructing high-resolution, patient-specific CT images from low-resolution clinical scans. The approach is grounded in the principles of Wolff's law and the bone remodeling process, capturing the underlying trabecular architecture of the femur. It assumes that a physiologically realistic bone structure should exhibit both high global stiffness and adequate mechanical stability. Accordingly, the method formulates an optimization problem that balances the minimization of compliance (i.e., maximized stiffness) with the incorporation of biological loading uncertainties, while simultaneously respecting local constraints imposed by the low-resolution CT data. The result is a refined and clinically interpretable trabecular structure.

Validation using a rabbit model and a large-scale femoral head region confirms the reliability and effectiveness of the proposed method. In practical, clinical-scale applications, the approach reconstructs detailed and biologically plausible trabecular networks, with a high feature similarity index of 93.6% with respect to the corresponding original CT images.

Compared to conventional topology optimization (TO) approaches, our method preserves more patient-specific morphological characteristics and significantly reduces the influence of imaging errors on key bone parameters. In contrast to data-driven image processing methods, it eliminates the need for pre-training and reliance on large datasets, thereby enhancing computational efficiency and improving practical applicability.

Overall, the integration of a robustness term helps to mitigate the effects of imaging artifacts, making the method particularly well-suited for clinical diagnostic settings. With its high efficiency and interpretability, the proposed framework holds promise for future deployment as a lightweight plugin tool for clinical use.

CRediT authorship contribution statement

Zeyang Li: Writing – original draft, Visualization, Validation, Software, Resources, Methodology, Investigation, Formal analysis, Data curation, Conceptualization. **Xuanxuan Huang:** Writing – original draft, Visualization, Validation, Software, Resources, Methodology, Investigation, Formal analysis, Data curation, Conceptualization. **Ziyun Ding:** Supervision, Methodology, Conceptualization. **Carol Featherston:** Supervision, Project administration. **Sam L. Evans:** Supervision, Project administration, Methodology. **Peter Zioupos:** Validation, Supervision, Resources, Project administration, Methodology, Formal analysis, Data curation, Conceptualization. **Zhangming Wu:** Writing – review & editing, Validation, Supervision, Resources, Project administration, Methodology, Investigation, Funding acquisition, Formal analysis, Conceptualization.

Ethics statement

The present study is a computational and image-based modelling investigation. The bone samples used in this work were provided by Prof. Peter Zioupos (University of Hull) on loan from Cranfield University (project id:20344; approval CURES-17613 on 28 Nov 2022; archaeological material collections). No new animal or human experiments were conducted for this study.

All procedures involving the existing bone samples were carried out in compliance with institutional and national ethical standards and relevant laws and guidelines. The study does not involve any direct experimentation on human or animal subjects, nor does it include any identifiable personal or clinical information. Therefore, additional ethical approval and informed consent were not required.

Declaration of competing interest

The authors declare that they have no known competing financial interests or personal relationships that could have appeared to influence the work reported in this paper.

Acknowledgments

The authors would like to express their sincerely thanks to Guang Li from Southeast University for providing CT and micro-CT images of the rabbit femur. Zeyang Li and Xuanxuan Huang would like to acknowledge the funding support from China Studentship Council and the tuition fee waiver studentship from Cardiff University. Zhangming Wu would like to acknowledge two awards from Marie Sklodowska-Curie Individual (Postdoctoral) Fellowships on the topic of topology optimization, and the funding support from the EPSRC research grant (EP/Y023455/1).

Appendix A. CT scan images collection and processing

In the experimental procedure, five femur specimens (Fig. A.1) were selected and scanned using the CurveBeam 4003 CT imaging system, as shown in Fig. A.2(a) and (b). Prior to scanning, the specimens were carefully cleaned and visually inspected to ensure there were no fractures or artifacts that could affect the reconstruction process. Each specimen was placed together in the scanner chamber, supported with low-density foam to minimize movement and avoid beam hardening artifacts during the scanning.

Since the samples were positioned manually, they were not aligned with the standard anatomical reference frame. This misalignment can lead to inconsistent slice orientation and complicate downstream modeling, which is then modified by the re-sliced by the MIMICS software in this work.

Table C.3
Mean value and variance of compliance for RTO and TO reconstructions across five samples.

Cases	RTO1	TO1	RTO2	TO2	RTO3	TO3	RTO4	TO4	RTO5	TO5
Mean Compliance (mJ)	4.73	3.16	2.01	1.21	1.34	0.40	2.26	1.43	4.58	8.76
Variance	0.68	2.39	0.19	0.34	0.08	0.04	0.26	0.73	0.99	4.02

Appendix B. Supplementary trabecular structural parameters

Additional structural parameters were quantified to provide a more comprehensive characterization, including connectivity density ($Conn.D$), degree of anisotropy (DA), and structure model index (SMI). Values for TO and RTO reconstructions across all samples are summarized in Table B.2. Consistent with the primary morphometric parameters, these supplementary metrics also reveal distinct patient-specific differences among samples, while demonstrating improved stability and reduced variability in the proposed RTO framework relative to conventional TO (paired comparisons confirm an average 28% reduction in overall variability). Notably, RTO exhibits more complex branch network, slightly lower anisotropy, and a structure closer to plate-like trabecular bone compared to conventional TO

Appendix C. FEM mechanical validation of reconstructed trabeculae

To verify the biomechanical reproducibility and mechanical performance of the reconstructed trabeculae, finite element (FE) analysis was performed on RTO and conventional TO reconstructed structures (five human femur samples) under 50 randomly perturbed gait loads (scaling factors A_i sampled from uniform distributions in Eqs. (7)–(9)).

FE validation results (as shown in Fig. C.1, Table C.3) confirm that RTO-reconstructed trabeculae exhibit superior mechanical robustness compared to TO (a low variation of compliance response under different loadings), while maintaining global stiffness relatively comparable to the level of TO ones. This biomechanical reproducibility of RTO confirms that the proposed RTO method effectively improves mechanical robustness metrics of trabecular structures.

References

[1] Utz Krug, Christoph Röllig, Anja Koschmieder, Achim Heinecke, Maria Cristina Sauerland, Markus Schaich, Christian Thiede, Michael Kramer, Jan Braess, Karsten Spiekermann, et al., Complete remission and early death after intensive chemotherapy in patients aged 60 years or older with acute myeloid leukaemia: a web-based application for prediction of outcomes, Lancet 376 (9757) (2010) 2000–2008.

[2] Robert W. Goulet, Steven A. Goldstein, Michael J. Ciarelli, Janet L. Kuhn, M.B. Brown, L.A. Feldkamp, The relationship between the structural and orthogonal compressive properties of trabecular bone, J. Biomech. 27 (4) (1994) 375–389.

[3] Huayue Chen, Xiangrong Zhou, Hiroshi Fujita, Minoru Onozuka, Kin-Ya Kubo, Age-related changes in trabecular and cortical bone microstructure, Int. J. Endocrinol. 2013 (1) (2013) 213234.

[4] Jung Jin Kim, In Gwun Jang, Image resolution enhancement for healthy weight-bearing bones based on topology optimization, J. Biomech. 49 (13) (2016) 3035–3040.

[5] In Gwun Jang, Il Yong Kim, Computational study of wolff's law with trabecular architecture in the human proximal femur using topology optimization, J. Biomech. 41 (11) (2008) 2353–2361.

[6] Roland Krug, Andrew J. Burghardt, Sharmila Majumdar, Thomas M. Link, High-resolution imaging techniques for the assessment of osteoporosis, Radiol. Clin. 48 (3) (2010) 601–621.

[7] Jisun Kim, Jung Jin Kim, Computationally efficient dominant load-based local bone microstructure reconstruction method using topology optimization, Comput. Biol. Med. 180 (2024) 108929.

[8] P.C. Shrimpton, M.C. Hillier, M.A. Lewis, M. Dunn, Doses from Computed Tomography (CT) Examinations in the UK, National Radiation Protection Board, Chilton England, 2003.

[9] Widya Mufida, Leny Latifah, Jeffri Ardiyanto, Digital image processing in CT scan facial bone with low mas to improve image quality and radiation dose reduction, in: International Conference on Health and Medical Sciences, AHMS 2020, Atlantis Press, 2021, pp. 109–112.

[10] S. Anand, R. Shantha Selva Kumari, Sharpening enhancement of computed tomography (CT) images using hyperbolic secant square filter, Optik 124 (15) (2013) 2121–2124.

[11] Indranil Guha, Syed Ahmed Nadeem, Chenyu You, Xiaoliu Zhang, Steven M Levy, Ge Wang, James C Torner, Punam K Saha, Deep learning based high-resolution reconstruction of trabecular bone microstructures from low-resolution CT scans using GAN-CIRCLE, in: Medical Imaging 2020: Biomedical Applications in Molecular, Structural, and Functional Imaging, vol. 11317, SPIE, 2020, pp. 204–214.

[12] Dinggang Shen, Guorong Wu, Heung-Il Suk, Deep learning in medical image analysis, Annu. Rev. Biomed. Eng. 19 (2017) 221–248.

[13] Geert Litjens, Thijs Kooi, Babak Ehteshami Bejnordi, Arnaud Arindra Adiyoso Setio, Francesco Ciompi, Mohsen Ghafoorian, Jeroen Awm Van Der Laak, Bram Van Ginneken, Clara I. Sánchez, A survey on deep learning in medical image analysis, Med. Image Anal. 42 (2017) 60–88.

[14] Jung Jin Kim, Jimin Nam, In Gwun Jang, Computational study of estimating 3D trabecular bone microstructure for the volume of interest from CT scan data, Int. J. Numer. Methods Biomed. Eng. 34 (4) (2018) e2950.

[15] Lijun Wang, Xiuling You, Lingli Zhang, Changqing Zhang, Weiguo Zou, Mechanical regulation of bone remodeling, Bone Res. 10 (1) (2022) 16.

[16] P.J. Prendergast, R. Huiskes, The biomechanics of wolff's law: recent advances, Ir. J. Med. Sci. 164 (1995) 152–154.

[17] S. Mohammad Ali Banijamali, Ramin Oftadeh, Ara Nazarian, Ruben Goebel, Ashkan Vaziri, Hamid Nayeb-Hashemi, Effects of different loading patterns on the trabecular bone morphology of the proximal femur using adaptive bone remodeling, J. Biomech. Eng. 137 (1) (2015) 011011.

[18] In Gwun Jang, Il Yong Kim, Byung Man Kwak, Analogy of strain energy density based bone-remodeling algorithm and structural topology optimization, J. Biomech. Eng. 131 (1) (2008) 011012.

[19] Harrie Weinans, Rik Huiskes, H.J. Grootenboer, The behavior of adaptive bone-remodeling simulation models, J. Biomech. 25 (12) (1992) 1425–1441.

[20] John W.C. Dunlop, M.A. Hartmann, Yves J. Bréchet, Peter Fratzl, Richard Weinkamer, New suggestions for the mechanical control of bone remodeling, Calcif. Tissue Int. 85 (2009) 45–54.

[21] Mengke Huo, Siyuan He, Yun Zhang, Yuxiao Feng, Jian Lu, Simulation on bone remodeling with stochastic nature of adult and elderly using topology optimization algorithm, J. Biomech. 136 (2022) 111078.

[22] D.R. Carter, David P. Fyhrie, R.T. Whalen, Trabecular bone density and loading history: regulation of connective tissue biology by mechanical energy, J. Biomech. 20 (8) (1987) 785–794.

[23] G.S. Beaupré, T.E. Orr, D.R. Carter, An approach for time-dependent bone modeling and remodeling—theoretical development, J. Orthop. Res. 8 (5) (1990) 651–661.

[24] Bong Ju Chun, In Gwun Jang, Determination of the representative static loads for cyclically repeated dynamic loads: a case study of bone remodeling simulation with gait loads, Comput. Methods Programs Biomed. 200 (2021) 105924.

[25] Ken-ichi Tsubota, Yusuke Suzuki, Tomonori Yamada, Masaki Hojo, Akitake Makinouchi, Taiji Adachi, Computer simulation of trabecular remodeling in human proximal femur using large-scale voxel FE models: Approach to understanding wolff's law, J. Biomech. 42 (8) (2009) 1088–1094.

[26] Junpeng Zhao, Chunjie Wang, Robust topology optimization under loading uncertainty based on linear elastic theory and orthogonal diagonalization of symmetric matrices, Comput. Methods Appl. Mech. Engrg. 273 (2014) 204–218.

[27] Xu Guo, Xiaofang Zhao, Weisheng Zhang, Jun Yan, Guomin Sun, Multi-scale robust design and optimization considering load uncertainties, Comput. Methods Appl. Mech. Engrg. 283 (2015) 994–1009.

[28] Carl-Johan Thore, Erik Holmberg, Anders Klarbring, A general framework for robust topology optimization under load-uncertainty including stress constraints, Comput. Methods Appl. Mech. Engrg. 319 (2017) 1–18.

[29] Kang Gao, Duy Minh Do, Sheng Chu, Gang Wu, H. Alicia Kim, Carol A. Featherston, Robust topology optimization of structures under uncertain propagation of imprecise stochastic-based uncertain field, Thin-Walled Struct. 175 (2022) 109238.

[30] Eelco Verhulp, Bert van Rietbergen, Rik Huiskes, Comparison of micro-level and continuum-level voxel models of the proximal femur, J. Biomech. 39 (16) (2006) 2951–2957.

[31] Jung Jin Kim, Youkyung Kim, In Gwun Jang, Estimation of local bone loads for the volume of interest, J. Biomech. Eng. 138 (7) (2016) 071004.

[32] M.O. Heller, Georg Bergmann, J.-P. Kassi, Lutz Claes, N.P. Haas, G.N. Duda, Determination of muscle loading at the hip joint for use in pre-clinical testing, J. Biomech. 38 (5) (2005) 1155–1163.

[33] J. Kerner, R. Huiskes, G. Harry van Lenthe, H. Weinans, Bert van Rietbergen, C.A. Engh, A.A. Amis, Correlation between pre-operative periprosthetic bone density and post-operative bone loss in THA can be explained by strain-adaptive remodelling, J. Biomech. 32 (7) (1999) 695–703.
[34] R. Ruimerman, P. Hilbers, B. Van Rietbergen, R. Huiskes, A theoretical framework for strain-related trabecular bone maintenance and adaptation, J. Biomech. 38 (4) (2005) 931–941.
[35] Jean-Marie Delaisse, Thomas Levin Andersen, Helene Bjoerg Kristensen, Pia Rosgaard Jensen, Christina Møller Andreasen, Kent Søe, Re-thinking the bone remodeling cycle mechanism and the origin of bone loss, Bone 141 (2020) 115628.
[36] Casey A. Myers, Peter J. Laz, Kevin B. Shelburne, Bradley S. Davidson, A probabilistic approach to quantify the impact of uncertainty propagation in musculoskeletal simulations, Ann. Biomed. Eng. 43 (2015) 1098–1111.
[37] Lars Larsson, Hans Degens, Meishan Li, Leonardo Salviati, Young Il Lee, Wesley Thompson, James L. Kirkland, Marco Sandri, Sarcopenia: aging-related loss of muscle mass and function, Physiol. Rev. 99 (1) (2019) 427–511.
[38] Andrew J. Teichtahl, Anita E. Wluka, Pushpika Wijethilake, Yuanyuan Wang, Ali Ghasem-Zadeh, Flavia M. Cicuttini, Wolff's law in action: a mechanism for early knee osteoarthritis, Arthritis Res. Ther. 17 (2015) 1–9.
[39] Martin Philip Bendsoe, Ole Sigmund, Topology Optimization: Theory, Methods, and Applications, Springer Science & Business Media, 2013.
[40] Kai Liu, Andrés Tovar, An efficient 3D topology optimization code written in matlab, Struct. Multidiscip. Optim. 50 (2014) 1175–1196.
[41] Jonah M. Dimnik, Kurt H. Wilde, W. Brent Edwards, Optimization of the density–elasticity relationship for rabbit hindlimb bones, J. Mech. Behav. Biomed. Mater. 163 (2025) 106882.
[42] Noor Abdalrazak Shnain, Zahir M. Hussain, Song Feng Lu, A feature-based structural measure: an image similarity measure for face recognition, Appl. Sci. 7 (8) (2017) 786.
[43] Timothy M. Ryan, Alan Walker, Trabecular bone structure in the humeral and femoral heads of anthropoid primates, Anat. Rec. 293 (4) (2010) 719–729.
[44] Eva Klintström, Örjan Smedby, Rodrigo Moreno, Torkel B. Brismar, Trabecular bone structure parameters from 3D image processing of clinical multi-slice and cone-beam computed tomography data, Skelet. Radiol. 43 (2) (2014) 197–204.
[45] Pouya Amiri, Anthony M.J. Bull, Prediction of in vivo hip contact forces during common activities of daily living using a segment-based musculoskeletal model, Front. Bioeng. Biotechnol. 10 (2022) 995279.
[46] Alexander Pürzel, Paul Kaufmann, Willi Koller, Elias Kaj Wallnöfer, Arnold Baca, Hans Kainz, Biomechanical analysis of hip, knee, and ankle joint contact forces during squats in elite powerlifters, PLoS One 20 (7) (2025) e0327973.
[47] M. Adeel Alam Shah, Shu-Jun Lü, Jian-Fei Zhang, Jia-Wei Wang, Wei Tang, Wen-Chao Luo, Hua-Xun Lai, Sheng-Bo Yu, Hong-Jin Sui, Functional morphology of trabecular system in human proximal femur: a perspective from P45 sectional plastination and 3D reconstruction finite element analysis, J. Orthop. Surg. Res. 20 (1) (2025) 370.
[48] Jeffry S. Nyman, Anuradha Roy, Xinmei Shen, Rae L. Acuna, Jerrod H. Tyler, Xiaodu Wang, The influence of water removal on the strength and toughness of cortical bone, J. Biomech. 39 (5) (2006) 931–938.
[49] Zeyang Li, Zhangming Wu, A novel multiscale design method for porous structures with tunable anisotropy: Varied-shape voronoi tessellation, Comput. Methods Appl. Mech. Engrg. 432 (2024) 117378.
[50] Jaejong Park, Alok Sutradhar, Jami J. Shah, Glaucio H. Paulino, Design of complex bone internal structure using topology optimization with perimeter control, Comput. Biol. Med. 94 (2018) 74–84.
[51] Greg M. Walter, Keyne Monro, Delia Terranova, Enrico La Spina, Maria Majorana, Giuseppe Pepe, James Clark, Salvatore Cozzolino, Antonia Cristaudo, Simon J. Hiscock, et al., Environmental effects on genetic variance are likely to constrain adaptation in novel environments, Evol. Lett. 8 (3) (2024) 374–386.
[52] Joshua D. Auger, Neilesh Frings, Yuanqiao Wu, Andre Gutierrez Marty, Elise F. Morgan, Trabecular architecture and mechanical heterogeneity effects on vertebral body strength, Curr. Osteoporos. Rep. 18 (6) (2020) 716–726.
[53] Xiuhong Huang, Liqin Zheng, Desheng Zheng, Shaobin Li, Yueguang Fan, Ziling Lin, Shaohong Huang, Studying trabecular bone samples demonstrates a power law relation between deteriorated structure and mechanical properties-a study combining 3D printing with the finite element method, Front. Endocrinol. 14 (2023) 1061758.